Supporting Information

Carlton et al. 10.1073/pnas.1004037107

SI Text

SI Materials and Methods *OMX: a fresh approach for wide-field microscopy.*

Overall concept.

It became clear that questions about dynamic chromosome motion in the nucleus required much higher temporal sampling (and resolution) than what the conventional microscope platform could deliver. Therefore, a fresh top-to-bottom microscope design and implementation was undertaken.

A recent quantitative review of all modern fluorescent microscope techniques (1) has shown that wide-field microscopy is the most efficient in photon collection, with spinning disk confocal microscopy at approximately 0.25 its sensitivity, followed by standard confocal microscopes at a factor of 0.01 – 0.005 the sensitivity of wide-field. Wide-field microscopy, using only an objective and a tube lens, and precise sequential positioning of the focal plane within the sample along the optical axis, collects a three-dimensional image (a Z stack) distorted by out-of-focus light. Constrained deconvolution returns out-of-focus light to its correct location (2). Four-dimensional in vivo microscopy must be able to operate under a large range of timescales, from minutes to milliseconds, corresponding to the wide variation in timescales of biological processes. Many interesting biological problems fall in the extremely rapid end of this range. For example, interphase chromosomes (3) and actin waves (4) exhibit motion in the subsecond range that is very difficult to acquire and study on current microscopes, usually limited, at best, to approximately one 3-dimensional image/sec. In addition, multiple colors (wavelengths) are usually acquired sequentially, making it difficult to quantitatively compare the position of differently labeled subcellular components at the same timepoint. Thus, the very fast four-dimensional platform we describe, capable of simultaneous recording of different wavelengths, will provide an important imaging modality well-suited for fast biological processes.

OMX addresses the shortcomings common to most commercial systems, and enables the implementation of many new features. With OMX live imaging we are able to collect ten three-dimensional images every second at four simultaneous wavelengths. In addition, this platform implements three-dimensional structured illumination (3D-SIM), allowing subdiffraction 100 nm xy and 200–300 nm z resolution (5, 6), as well as single-molecule localization microscopy capability (PALM, STORM, etc.).

There were several design considerations. First, we wanted to use a new microscope design to incorporate features that might be especially important to future cell biology, especially the imaging of whole organisms or tissues. Tissues contain many potentially identifiable cell types in a 3-dimensional arrangement. A commonly encountered problem is rapidly finding small pieces of tissue scattered over the cover-slip, or finding one sample of interest out of hundreds of similar tissue pieces on the cover-slip. Secondly, the new microscope platform must collect very fast subsecond 3-dimensional data cubes at multiple simultaneous wavelengths for sustained periods of time. Thirdly, the microscope had to have high-sensitivity electron multiplying (EM) CCDs so that every possible photon could be counted. Coupled with these features, all the optics had to be designed with minimization of stray-light to achieve the highest signal-to-noise data. Fourthly, the microscope had to be extremely stable, drifting only tens of nanometers per minute, using precision technology.

An entire room, approximately 200 ft^2 (in our case 10×20) comfortably houses this microscope system (Fig. S3). Broadly speaking, OMX consists of three parts:

First, there is a separate low magnification microscope station used for sample location, the LMX microscope. This subsystem is built around a Kramer M2, a Zeiss upright dissecting microscope body with Kramer fluorescence capability and metallurgical objectives, producing high resolution images at very high working distances. A CCD is provided for continuous scanning. The motorized xy-stage is encoded with submicron capability and these positions are cross-indexed with OMX itself. We wrote custom software to allow building an image mosaic covering a whole 22×22 mm cover slip (Fig. S4). Extended sensitivity and resolution by averaging and/or integrating over times are possible. This auxiliary microscope can then find objects of interest for further data analysis by OMX.

The second subsystem is the laser light source. Solid-state laser sources are very bright (typically 100 + mW), with high stability (better than 1 part in 1000 intensity stability) over the short and long term, long-lived, and easy to launch into fiber optic cables leading to the OMX microscope itself. Currently we are using 403 nm, 488 nm, 532 nm, 560 nm, and 642 nm lasers. These are gated by laser shutters (also beam traps when shutter is closed) for fast 150 Hz shuttering (nmLaser LST200) followed by a computer driven filter wheel (Thorlabs FW902) with a series of dielectric intensity stable neutral density filters (CVI laser). Then the light is parsed by extremely stable pop-up mirrors (New Focus 8892), under computer control to send the light to either conventional wide-field illumination or structured illumination, or a complex closed-loop piezo-aligned single-mode laser launch device (Thorlabs NanoTrak/BNT001) so that all laser lines can be optimally launched into the single-mode fiber for TIRF. Finally the coherence of the laser light is scrambled by a rapidly rotating light shaping diffuser (Luminit, formerly Physical Optics, model LSD5GL1) to minimize laser speckle.

The third subsystem is OMX itself, which consists of several components. The first component is a clean room enclosure approximately $5 \times 5 \times 8$ ft. The enclosure is light tight, class 100 (when purged and people free for a few hr), prefiltered with charcoal filters to remove coarse and fume/odor laden air, with acoustic dampening/isolation. The enclosure exists in a conventional air-conditioned room (22.3 °C, with ~0.5° temperature stability), but the HEPA fan unit, providing positive pressure, buffers the temperature fluctuation to ~0.01–0.03 °C over many hours. Whereas the enclosure was designed to throttle the fan motor down to reduce vibration and use PID solid-state air conditioner for ultimate temperature stability, we have not used these design features. The enclosure is designed for users to open the door, (automatically turning on the room light) place the sample on OMX, and close the door (turning off the light). Subsequent interaction with the sample, through the use of CCDs, takes place at the console/visualization station.

Inside the enclosure, OMX sits on a Newport vibration isolation 4 inch damped (SG series) breadboard-table. OMX is machined out of a solid block of 7075 stressed-relieved aluminum, solidly bolted to the table, and purged with positive pressure filtered (0.45 μ) dry nitrogen for moisture control of the dichroic and emission filters. Extensive care in the OMX design was made for minimizing stray-light and for utmost stability. Zerodur, a highly temperature invariant and insulating ceramic, was used for kinematic mounting of the single objective and the stage. Movement of the stage over a 1-inch cube in x, y, z uses a Newport 462 series interferometer grade stage, encoded microstepper stage motors and incorporated closed-loop piezoelectric motors (Piezosystem Jena) in each axis. An alignment laser is

permanently embedded into the OMX system to be able to align the optics and to periodically check for alignment drift at several places in the optics layout.

All the essential beam-splitting dichroic mirrors are housed in a kinematically mounted removable drawer module. Each dichroic mirror is alignable in two degrees of freedom from the front of the drawer allowing precise coregistration of the different wavelength images. Again careful attention to stray-light suppression was made.

The computer hardware for OMX is distributed over nine Windows based computers. The computers are connected to a local network switch for fast easy-to-implement communication. Each CCD camera has its own computer with the capability to perform a "gain and offset" correction of the CCD image on-the-fly, and normalizes the baseline so that image intensity is stable as a function of time. Another computer handles low-resolution x, y, z position, DIC z position, multiple temperature readout, TIRF angle position, and some diagnostic features. LMX and the single-mode TIRF fiber system each has its own computer. The master computer runs the acquisition and display software plus data storage. The overall control is a DSP computer that supplies analog voltage modulation for the piezo control, TTL lines for all cameras, shutters etc., leading to a precise sequencing of image acquisition events.

The last aspect of OMX itself is the software. An early part of the software design was the incorporation of a flexible scripting language (Python) that would be fast, well-supported (heavily used in the astronomy community), and easily modified and maintained. We also wanted extensive documentation, a worldwide network database for bug fixes, and local expertise (the UCSF computer graphics group of Tom Ferrin). We also wanted the software to be open and freely distributable so that all users would modify and extend the software. We wanted the software for image acquisition to have a series of "instruments," under software control, so that the user could navigate in 3 and 4D space as the data was collected. The user could see what was being collected at all wavelengths with every image displayed and the ability to scale these dynamically on-the-fly. There were to be auto-focus software instruments, as well as intuitive position reporting in x, y, z. In addition, there was to be extensive mosaic image capability that would be synchronized with LMX.

The four modalities of OMX.

OMX can be used in any of four imaging modalities. All four modalities make use of OMX's stability, fast timing and precision sequencing of image acquisition.

Fast live.

The first OMX modality is its fast live imaging capability. Several technological advances make it possible for OMX to collect very fast three-dimensional data. At the top of the list is the master timer, the digital signal processor (DSP). This computer board, in a regular PC, allows for deterministic events to be sequenced to a series of buffered TTL lines going to the cameras, shutters, and lasers. In addition the DSP has a number of 16-bit digital to analog voltage lines that modulate the piezo channels. The DSP is programmed in a template format so that it is very easy to modify the acquisition process to add features or tune the data collection process. The next important feature, crucial to fast data collection, is the closed-loop piezo device that moves the 3 axes of the stage. This fast, stable, precise, smooth motion device moves the Z stage in a triangular ramp for focus, utilizing both the up and down aspects of the triangular wave motion. The piezo axis control also allows for the possibility of biological sample drift control. The capabilities of the fast live modality are featured in the accompanying paper.

3D structured illumination microscopy (3D-SIM).

The second OMX microscope modality is 3D-SIM, described in (5). Its main advantages are increased spatial resolution, up to 100 nm laterally and 250 nm axially, and its ability to be routinely used on diverse biological samples.

3D TIRF.

The third OMX modality is total internal reflection fluorescence microscopy (TIRFM). Laser light at multiple wavelengths is launched into a single-mode fiber by use of a Thorlabs piezoelectric tracking and feedback device (BNT001/Nanotrak). The other end of the single-mode fiber, at the OMX microscope, is coupled to a stable closed-loop motorized stage (Newport 462 XYZ) together with a Physik Instrumente 40 μm closed-loop piezo stage so the emitted single-mode light reproducibly enters the back focal plane of the objective at a precisely defined point, and emerges at the critical angle for total internal reflection. With precise control of the fiber position, a range of TIRF angles are possible, allowing depth modulation of the evanescent wave (7).

PALM.

PALM and related techniques (8–13) have enabled 20 nm resolution of specific biological substructures. PALM is based on widefield microscopy and thus can be successfully applied to our OMX platform, and represents the fourth modality.

PALM needs specialized software, and an important feature of our OMX software is its customizability. The software is now modified to allow excitation/activation cycles for stochastic activation/switching of fluorophores. The programmed shutter and camera sequence is sent to the DSP control for fast execution. An acquisition series consisting of 20,000 512×512-pixel images taken at 30 msec exposure time with multiple wavelengths takes about 13–30 min to finish depending on the number of activation images. The activation and excitation can be multiple wavelengths and the duration of any of these can be progressively changed during data acquisition if necessary.

The design of the dichroic mirror drawer system in OMX greatly facilitates PALM 3D reconstruction. Multiplane PALM is possible using combinations of four cameras, additional lenses and beam splitters. Astigmatism is induced by installing cylindrical lenses in the drawer, or by flexing the dichroic mirrors with tightening screws. Users of the microscope can simply switch drawers when needed. Whereas both multiplane and astigmatism PALM methods have 50–100 nm axial precision for bright organic dyes (12, 13), dimmer fluorescent proteins are not successfully reconstructed with such accuracy. In that case, piezoelectric control of the OMX stage is far more accurate, as long as fluorescent proteins continue to fluoresce.

The stage has very low drift, allowing short data acquisition (<3 min) without drift correction. For longer acquisition, we use another channel for drift correction (e.g. DAPI staining of chromatin) because multiple wavelengths can be simultaneously collected. The drift is measured by cross correlation and corrected by our PALM reconstruction program. Lateral stage drift is usually within 80 nm/10 min.

PALM is essentially single-molecule imaging within biological samples. Therefore, unless the sample is an ideal material for single-molecule imaging, background noise diminishes Gaussian peaks, resulting in low-resolution reconstruction (~100 nm accuracy is common even with 1,000 photon yield in the presence of lots of background). Thus, removing noise is the most important aspect in performing PALM with real biological structure.

TIRF has been a preferred mode to remove out-of-focus light if the object of interest is within the evanescence field (~100 nm from the cover slip in conventional TIRF mode). As already described above, our TIRF settings allow the depth of the evanescent wave to be precisely set up to ~500 nm. The illumination angle can go lower than the critical angle, resulting in another

optical modality of highly inclined laminated sheet optical microscopy, which also has an advantage in removing out-of-focus light (14). We found that high NA (>1.40), high magnification objective lenses (×100, ×150) have a rather shallow depth of field, and thus as long as refractory index mismatch is low (i.e. sample is close to the cover slip), standard wide-field microscopy without TIRF is often good enough for single-molecule analysis. Lateral background fluorescence is removed by computer-controlled field apertures.

The denoising algorithm reported here has been successfully used for cleaning up the raw single-molecule images. This speeds up the processing time of PALM reconstruction up to 100 times depending on the noise level. The image is further high-pass filtered to remove low frequency background noise and for individual molecules to stand out. We use 2D iterative deconvolution for this high-pass filter. Because localization accuracy depends both on noise and width of the point spread function (PSF) (and other factors), denoising and deconvolution improves localization accuracy. Denoising and deconvolution also improves final point density (AM, DAA, JWS, manuscript in preparation) by helping PSFs to stand out. The combined effect of these processing steps with our usual chromosome samples results in approximately fourfold improvement in resolution by increasing localization accuracy and point density.

Photon detection and photo-electron shot-noise. Cell viability is inversely related to the dosage of excitation light exposure. On the other hand, a low dosage of excitation light can cause low signal-to-noise in the raw image data, and can thus severely affect the quality of the microscopy image processing. In this supplement, we discuss this trade-off due to the limitation coming from the photo-electron shot-noise of the electron multiplying charge coupled device (EMCCD) data.

The lowest level of light excitation that can be adequately used depends greatly on the sensitivity and efficiency of the imaging system, the fluorophore density, and the number of photons emitted by the fluorophore at each exposure. For example, EGFP has a molar extinction coefficient $(\varepsilon) = 56{,}000$ liter/Moles · cm at 488 nm (15). This is equivalent to an absorption cross-section $(\sigma) = 3.82 \times 10^{-21}\varepsilon$ cm^2, or 2.14×10^{-8} μm^2. The quantum yield of fluorescence for EGFP is 0.60. The quantum efficiency of the Andon iXon+ EMCCD camera at the EGFP emission band (510 ± 15 nm) is 0.95 (http://www.andor.com). At NA = 1.4 high resolution imaging on OMX, light rays emitted in a fraction 0.3 of the 4π solid angle will be collimated through the imaging optics with a light throughput efficiency (due to absorption and reflection losses) of ~0.6. The resulting effective PSF volume in the sample space is shaped like a prolate spheroid with dimensions approximately 200 nm and 600 nm. This volume can contain anywhere of the order between 10 to 100 EGFP molecules, due to the variation in the high copy number of the LacO array. For this calculation we use a conservative geometric average of 30 fluorophores. With a 200x magnification imaging (100x objective), at focus in the CCD image plane, the PSF is effectively spread over 9 pixels (3×3). With the maximum excitation exposure of 488 nm laser light at $I = 5 \times 10^{-4} I_0$ for 10 msec, a simple rate calculation, that ignores the relatively smaller effect of the triplet state branching and quenching, shows the total number of photo-electron generated per CCD pixel is approximately equal to 5, with a shot-noise of $\mathrm{sqrt}(1/5) = 45\%$. The electron multiplication process of the EMCCD increases the shot-noise by a factor of sqrt (2), thus the electron shot-noise becomes 63%. This gives a rather quite low signal-to noise-ratio (S/N) equal to 1.6.

To overcome this low S/N problem, the denoising algorithm assembles the signal from the resolution limited spot of 3× 3 pixels, effectively multiplying the raw data S/N by a factor of $\mathrm{sqrt}(3 \times 3)$, giving a reconstruction with S/N ratio of 4.8, enough to computationally boost the signal beyond the noise floor to reconstruct the true image.

1. Wolf DE, Samarasekera C, Swedlow JR (2007) Quantitative analysis of digital microscope images. *Meth Cell Biol* 81:365–396.
2. Hiraoka Y, Sedat JW, Agard DA, (1990) Determination of three-dimensional imaging properties of a light microscope system. Partial confocal behavior in epifluorescence microscopy. *Biophys J* 57:325–333.
3. Vazquez J, Belmont AS, Sedat JW (2001) Multiple regimes of constrained chromosome motion are regulated in the interphase Drosophila nucleus. *Curr Biol* 11:1227–1239.
4. Millius A, Dandekar SN, Houk AR, Weiner OD (2009) Neutrophils establish rapid and robust wave complex polarity in an actin-dependent fashion. *Curr Biol* 19:253–259.
5. Schermelleh L, et al. (2008) Subdiffraction multicolor imaging of the nuclear periphery with 3D structured illumination microscopy. *Science* 320:1332–1336.
6. Gustafsson GL, et al. (2008) Three-dimensional resolution doubling in wide-field fluorescence microscopy by structured illumination. *Biophys J* 94:4957–4970.
7. Mattheyses AL, Axelrod D (2006) Direct measurement of the evanescent field profile produced by objective-based total internal reflection fluorescence. *J Biomed Opt* 11:014006.
8. Betzig E, et al. (2006) Imaging intracellular fluorescent proteins at nanometer resolution. *Science* 313:1642–1645.
9. Rust MJ, Bates M, Zuang X (2006) Sub-diffraction-limit imaging by stochastic optical reconstruction microscopy (STORM). *Nat Methods* 3:793–795.
10. Bock H, et al. (2007) Two-color far-field fluorescence nanoscopy based on photoswitchable emitters. *Appl Phys B-Lasers O* 88:161–165.
11. Hess ST, Girirajan TP, Mason MD (2006) Ultrahigh resolution imaging by fluorescence photoactivation localization microscopy. *Biophys J* 91:4258–4272.
12. Huang B, et al. (2008) Three-dimensional superresolution imaging by stochastic optical reconstruction microscopy. *Science* 319:810–813.
13. Juette MF, et al. (2008) Three-dimensional sub-100 nm resolution fluorescence microscopy of thick samples. *Nat Methods* 5:527–529.
14. Tokunaga M, Imamoto N, Sakata-Sogawa K (2008) Highly inclined thin illumination enables clear single-molecule imaging in cells. *Nat Methods* 5:159–161.
15. Lakowicz JR (2006) *Principles of Fluorescence Spectroscopy* (Springer, New York, 3rd Ed).

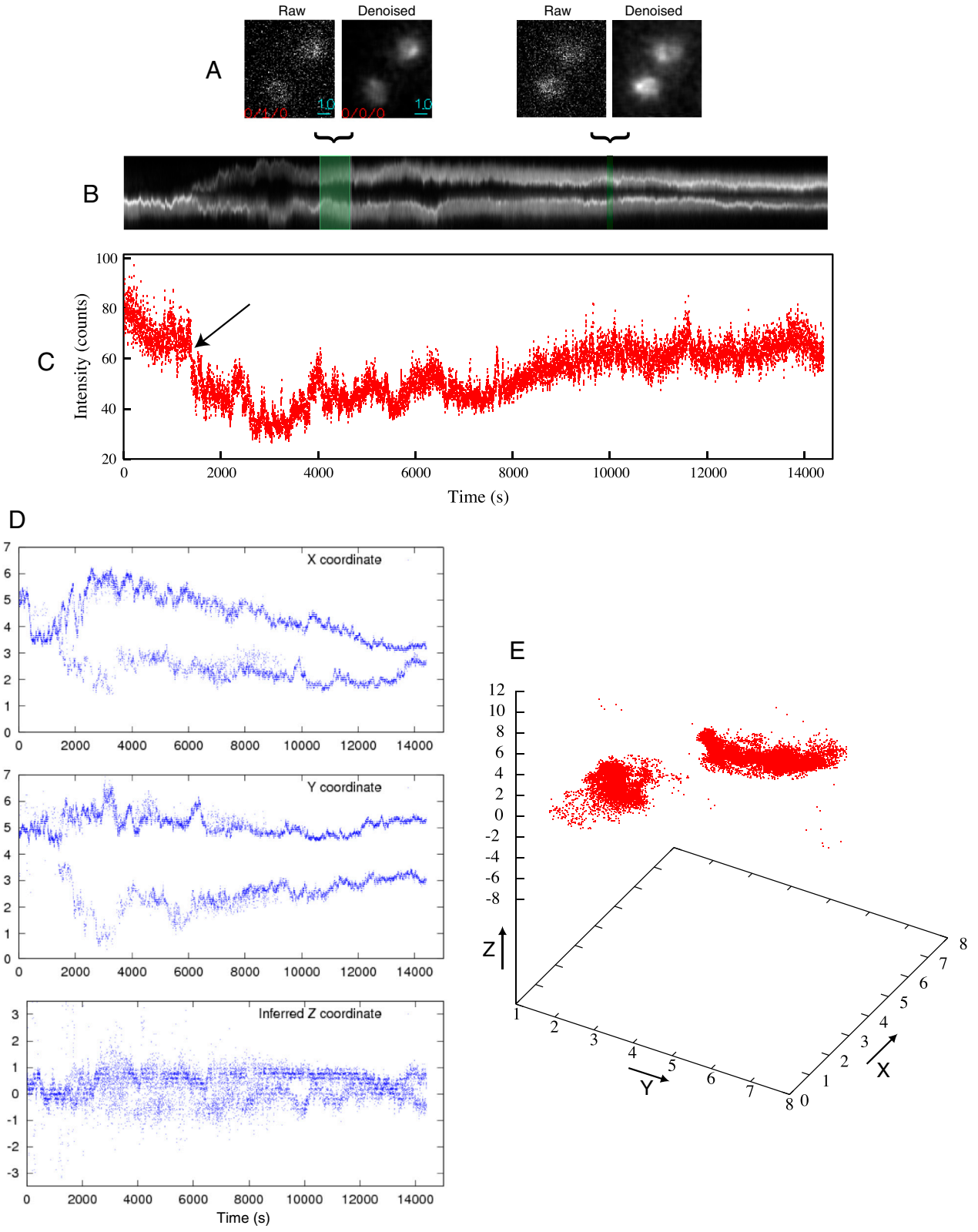

Fig. S1. 3D tracking over time in low-light-level images in dense-regime imaging. (*A*) individual frames from image series selected from indicated timepoints. (*B*) Kymograph of denoised images over the entire 2 h period. Region highlighted in green, corresponding to the left side of *A*, is contained in Movie S4. (*C*) The intensity of one tracked point continuously present in the mother cell (at bottom in kymograph) is shown. Note drop in intensity at the point of cell division (arrow) and subsequent increase to predivision level. (*D*) the X, Y, and inferred Z (see Fig. S2) coordinates, in microns, of each point. (*E*) Tracked points displayed in 3D demonstrate the extent of movement.

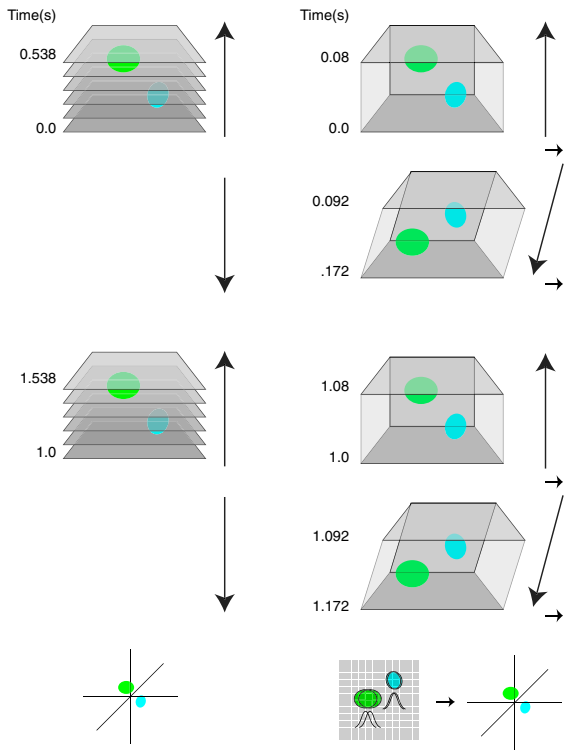

Fig. S2. Diagram of stereo-projection imaging for 3D tracking of point-like objects. (*Left*) Conventional Z stack imaging of two points in the dense-regime. The shutter is closed in between each image acquisition, and the stage moves while the camera is being read out. Collecting 25 sections with 10 msec exposures and 12 msec readout time requires 538 msec to collect an entire Z stack. The next Z stack begins 462 msec after the last acquisition of the previous Z stack, at $T = 1$ sec. The 3D positions of the spots are temporally blurred over a period of 538 msec, but are directly available in the Z stack. In contrast, with projection imaging, the shutter opens for 80 msec, during which time the stage is moved through the entire Z stack, resulting in an average-projection of the 3D image. The shutter is then closed while the camera is read out and the stage moves to the right. Another projected Z stack is immediately acquired with the stage moving in the opposite direction in Z, as well as to the left. Acquisition of both images requires 172 msec. The second Z projection image is slightly spread out in the X direction, causing the recorded X position of imaged foci to depend on their location in Z: higher foci will be shifted to the right, and lower foci will be shifted to the left. The distance offset between the same point in both directions is measured by Gaussian fitting, and multiplied by the ratio between the Z and X stage movements to obtain the Z position.

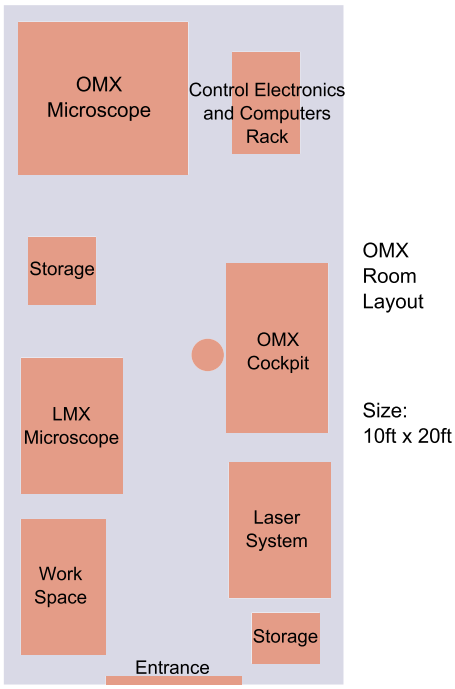

Fig. S3. OMX room figure. The layout of the room containing the OMX microscope and associated hardware.

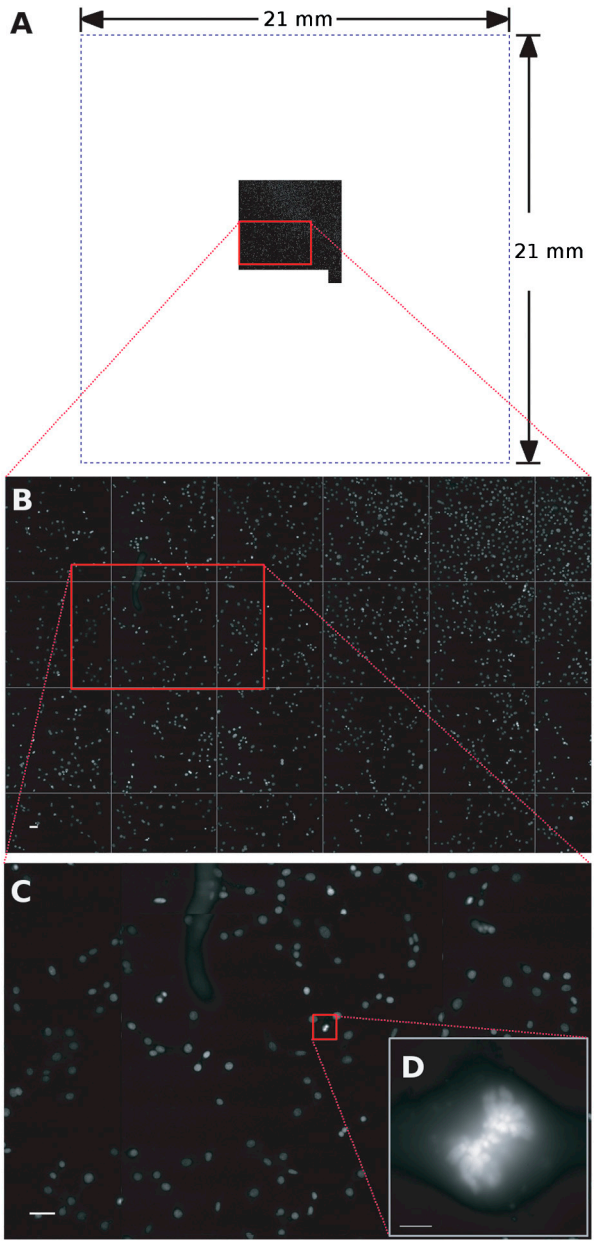

Fig. S4. Mosaic images from the auxiliary microscope LMX. A representative mosaic view of fixed 3T3 cells stained with DAPI. (*A*) Entire coverslip view (blue box is a square of 21 × 21 mm) at zoom 0.04. (*B*) Magnified view of boxed region in (*A*) at zoom 0.33. Individual 1024 × 1024 pixel images are highlighted with gray grids. (*C*) Magnified view of the boxed region in (*B*) at zoom 1.0 (pixel size 0.6152 μm). (*D*) An optical section from 3D stack of a metaphase chromosomes boxed in (*C*) taken with OMX (pixel size 0.0792 μm). Bar is 50 μm in (*B*) and (*C*), and 5 μm in (*D*).

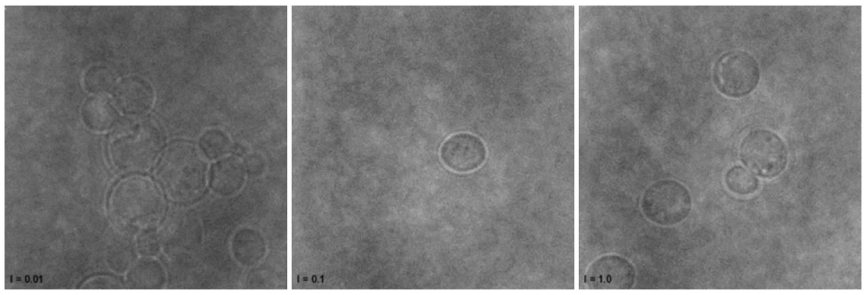

Movie S1. Yeast cells imaged with brightfield (fluorescent room light) every 15 min for an 8.5 h period after undergoing sparse imaging at $I = 10^{-2} I_0$ (*Left*), $I = 10^{-1} I_0$ (*Center*), or $I = I_0$ (*Right*). All cells were located on the same agarose pad within 1 mm of each other. The cells at left show unperturbed growth; the middle cell shows limited growth after a delay; whereas the cells at right do not grow at all.

Movie S1

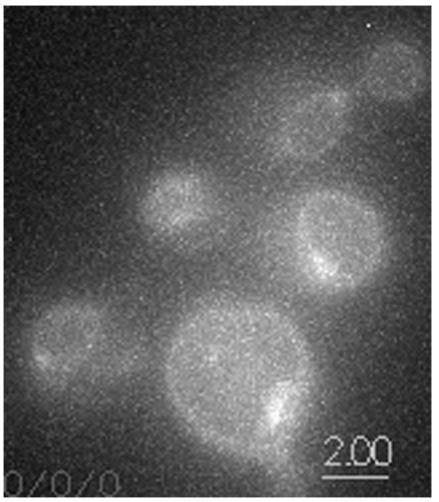

Movie S2. Average-projection images of strain S0992b containing GFP:$FYVE_{EEA1}$ is imaged in the dense regime at $I = 10^{-3} I_0$. Whereas wild-type cells imaged at this intensity survive, GFP-containing cells failed to divide after imaging.
Movie S2

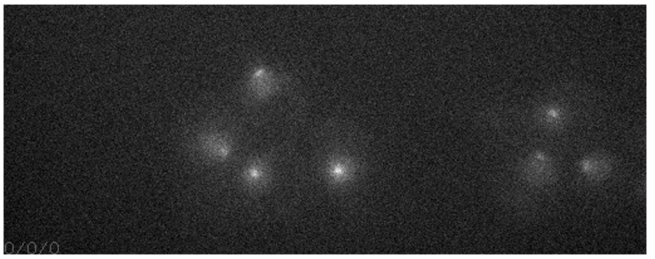

Movie S3. Yeast cells (strain YDB271) from still image in Fig. 7, imaged in projection mode in the Dense-regime (1 3D image per second) at $I = 5 \times 10^{-4} I_0$. Each frame is a time-average of 30 s.
Movie S3

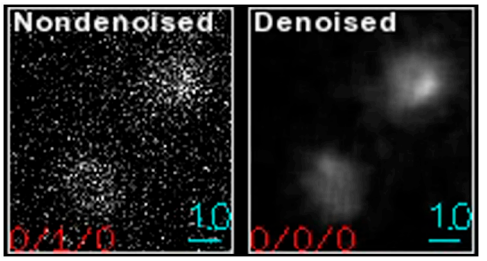

Movie S4. Yeast cells (strain YDB271) under 2.5D stereographic parallax imaging mode at $I = 5 \times 10^{-4} I_0$. Raw single projections with constant X stage position are shown at left, whereas the denoised version of the same image is shown at right. The span of this movie over the full 2 h of recording is indicated in by the transparent green overlay on the kymograph in Fig. S1(*B*).
Movie S4

Table S1. Excitation light attenuation values

$\lambda = 488$ nm

Power attenuation (OD)	Power (mW)*	Intensity (mW/μm^2)	Intensity (mW/pix^2)	Photons/μm^2 · sec	Photons/pix · sec
0	7.86E+01	4.78E−02	3.00E−04	1.17E+14	7.35E+11
1	7.30E+00	4.44E−03	2.79E−05	1.09E+13	6.83E+10
2	8.60E−01	5.23E−04	3.28E−06	1.28E+12	8.04E+09
3	7.89E−02	4.80E−05	3.01E−07	1.18E+11	7.38E+08
4	8.52E−03	5.18E−06	3.25E−08	1.27E+10	7.97E+07
5	1.00E−03	6.08E−07	3.82E−09	1.49E+09	9.35E+06

$\lambda = 532$ nm

Power attenuation (OD)	Power (mW)*	Intensity (mW/μm^2)	Intensity (mW/pix^2)	Photons/μm^2 · sec	Photons/pix · sec
0	9.63E+01	5.86E−02	3.67E−04	1.57E+14	9.82E+11
1	8.17E+00	4.97E−03	3.12E−05	1.33E+13	8.34E+10
2	1.41E+00	8.58E−04	5.38E−06	2.29E+12	1.44E+10
3	1.22E−01	7.42E−05	4.66E−07	1.98E+11	1.24E+09
4	2.13E−02	1.30E−05	8.13E−08	3.46E+10	2.17E+08
5	4.15E−03	2.52E−06	1.58E−08	6.75E+09	4.23E+07

*Power values were measured at the objective back focal plane; intensity values calculated for the sample plane.